X-ray imaging plate performance investigation based on a Monte Carlo simulation tool

M. Yao, Ph. Duvauchelle, V. Kaftandjian, A. Peterzol-Parmentier, A. Schumm

X-ray imaging plate performance investigation based on a Monte Carlo simulation tool

M. Yao[a], P. Duvauchelle[a], V. Kaftandjian[a], A. Peterzol-Parmentier[b], A. Schumm[c]

[a]*Laboratoire Vibration Acoustique (LVA), INSA de Lyon, 25 Avenue Jean Capelle, 69621 Villeurbanne Cedex, France*
[b]*AREVA NDE-Solutions. 4 Rue Thomas Dumorey, 71100 Chalon-sur-Saône, France*
[c]*EDF R&D SINETICS. 1 Avenue du Général de Gaulle, 92141 Clamart Cedex, France*

Abstract

Computed radiography (CR) based on imaging plate (IP) technology represents a potential replacement technique for traditional film-based industrial radiography. For investigating the IP performance especially at high energies, a Monte Carlo simulation tool based on PENELOPE has been developed. This tool tracks separately direct and secondary radiations, and monitors the behavior of different particles. The simulation output provides 3D distribution of deposited energy in IP and evaluation of radiation spectrum propagation allowing us to visualize the behavior of different particles and the influence of different elements. A detailed analysis, on the spectral and spatial responses of IP at different energies up to MeV, has been performed.

Keywords: Monte Carlo simulation, Computed Radiography, Imaging Plate Performance, High energy applications

1. Introduction

Computed radiography (CR) system, based on the use of an imaging plate (IP) composed of photostimulable phosphor (PSP) powder embedded in organic binder, is one of the efficient digital replacement techniques of the traditional conventional film radiography [1, 2]. Aside from keeping the advantage of the traditional radiography such as flexibility of the detector, CR brings other advantages, which are direct digital readout image, reusability of the detector, elimination of the developing process with chemical product, reduction in exposure (through great sensitivity of IP) and dynamic range larger than 5 orders of magnitude in X-ray dose [3, 4, 5, 6].
CR proves good performance within low energy range, but regarding the high energy range (up to MeV), which is also normal working energy range for industrial inspection of high attenuation objects, CR image quality is poor. The reason is that IP response is poor to the direct beam which carries the sharp geometry information of the object, but sensitive to secondary beam emerging from the object which is responsible for blurring. This issue has already been addressed for film radiography by the use of metallic screens which increase the dose received in the film thanks to secondary radiations occurring in the screen. Metallic screens should be placed in contact with the film so that emitted electrons can reach the argentic emulsion of the film. As far as IP is concerned, the use of metallic screens is also requested at high energies by current standards, so that the high energy photon beam could be rendered into electrons and lower energy photons, to which IP is more sensitive [7, 8]. However, the commercial IPs are usually comprised of a protective layer coated on phosphor layer to provide protection against normal handling, and this layer might prevent the rendered photon or electron from entering the phosphor layer.
As regards the spatial resolution, the metallic screens also further spread the incident beam, which means that a compromise should be found between intensifying the signal (by increasing the screen thickness) and improving spatial resolution. Moreover, when compared with film radiography, the spatial resolution is further degraded due to the light scattering at the phosphor grains during readout process [2, 3].
In order to follow the interactions involved in the metallic screen and IP detector system, a Monte Carlo simulation is of particular interest. It can give insight on physical phenomena which is difficult or impossible to observe experimentally, such as scattering effect, spatial distribution of deposited energy, K absorption and K fluorescence reabsorption.
Monte Carlo simulation has already been applied for system performance study and optimization as well as experimental result prediction in a number of studies [9, 10, 11, 12, 13, 14, 15, 16, 17, 18, 19, 20], but lots of these works were conducted for medical application. Though in some works [17], [18] and [20], the spectral response of IP material and the spatial response to certain irradiation sources have been reported, there is still a lack of the detailed spatial response characterization up to high energies (MeV). Moreover, in all previous studies, the IP system is studied alone, without taking into account the object under test. At high energies, the object is responsible for a huge amount of secondary radiation, which is not a useful part of signal as regards defect detection, and thus, image quality optimization consists in not only increasing the amount of deposited energy due to the direct beam (*useful signal*), but also decreasing the deposited energy due to the secondary beam. Direct and secondary beams must here be understood at the object level.
For the purpose of understanding how the relevant operating parameters affect the X-ray image and optimizing the image quality supplied by CR system, we have developed a Monte Carlo simulation tool based on PENELOPE [21]. This tool

tracks separately the direct and secondary as well as photon and electron radiations. The present paper will show the use of this tool through an optimization study of a realistic inspection case. The optimization was carried out by first characterizing the response of different combinations of IP and screens. The detector response has been analyzed in terms of performance metrics such as energy absorption efficiency (EAE) and modulation transfer function (MTF) for various incident energies up to 1.3 MeV.

2. Simulation tool and performance metrics

2.1. Simulation method

Our simulation tool is based on the PENELOPE subroutine package, and involves a classical situation of radiography with a radiation source, an object and a detector. Here, by detector we mean the combination of IP and metallic screens since the purpose of these screens is to optimize the IP response. All physical effects are taken into account in the simulation: photoelectric effect, Compton and Rayleigh scattering, pair production, as far as photons are concerns. For electrons and positrons, Bremsstrahlung emission, elastic and inelastic scattering as well as positron annihilation are considered.

The geometry adopted is shown in Figure 1(a), as well as the terms employed for the different beams issued from the object under test. After the object, the solid arrow represents the direct radiation, i.e., the part of photons which did not undergo any interaction, and all radiation produced from this beam in the following is called the $useful$ beam. On the contrary, the dashed arrow represents the secondary radiation issued through the object, and all further radiations produced are denoted as $not\,useful$. The information is subdivided into the signals due to the photons in the $useful$ beam or $not\,useful$ beam (denoted as UPS and NUPS), the electrons in the $useful$ beam or $not\,useful$ beam (denoted as UES and NUES), and, if any, the positrons in the $useful$ beam or $not\,useful$ beam (denoted as UPoS and NUPoS).

All the different particles (photons/electrons/positrons respectively $useful$/$not\,useful$) are tracked and registered separately during the Monte Carlo simulation process. For each of these particles, the simulation monitors two kinds of signals: the deposited energy distribution inside the IP and the step-by-step transmitted spectra after each element between source and IP (Figure 1(b)). A uniform three-dimensional orthogonal grid is used to sample the IP in such a way that the energy deposition distribution is recorded in 3D. For this reason, the IP geometry should be cuboid.

The incident beam could be either diverging or not, emitted from a point or an extended source, and its spectrum can be specified (such as that emitted from a cobalt or iridium source) or be a fixed energy varying within a specified range $\{E_{min}\,;E_{max}\}$ with an increment of E_{incmt}. The object and metallic screens could be of arbitrary material and geometry.

In all the following, the IP was modeled as a multi-layered structure which is comprised of, in sequence, a 6 μm protective layer, a 150 μm phosphor layer, a 254 μm support layer and a 25.4 μm backing layer. The materials of these four layers are respectively Mylar for the protective and support layers, $BaFBr:Eu^{2+}$ with a packing factor of 60% for the phosphor layer, and polycarbonate for the backing layer. As the phosphor layer is the actual effective layer for information storing, the orthogonal grid was applied to the phosphor layer for energy deposition distribution recording.

2.2. Performance metrics

The following outputs are available from our simulation tool:

- 3D deposited energy due to each kind of beam and each kind of particle:
  - Useful photon signal $DEP_{UPS}(x,y,z)$;
  - Not useful photon signal $DEP_{NUPS}(x,y,z)$;
  - Useful electron signal $DEP_{UES}(x,y,z)$;
  - Not useful electron signal $DEP_{NUES}(x,y,z)$;
- Transmitted photon spectra after different elements (i.e. object, metallic screens and IP protective layer);
- Transmitted electron spectra after different elements.

From these outputs, the following metrics are used to investigate the IP response under different simulation configurations:

- Energy absorption efficiency (EAE). It is the fraction of X-ray energy absorbed in IP, and is calculated as the total energy deposited in IP divided by the incident beam energy. Here, the total energy is considered, i.e. the sum of all signals due to all particles. If needed, $useful$ versus $not\,useful$ energy can be separated (see the results section).
- Fraction of deposited energy due to electron beam (f_{ElDep}). The f_{ElDep} is calculated as the ratio of the deposited energy due to electrons into IP over the total deposited energy in IP. Note that the electron beam is produced by the metallic screens.
- Modulation Transfer Function (MTF) and spatial frequency at 20% MTF (f_{MTF20}). The MTF is a basic metric to express the system spatial resolution. It is calculated as the modulus of the Fourier transform of the Point Spread Function (PSF) normalized to unity at zero spatial frequency. In practice, the Line Spread Function, describing the system response to a line, is usually measured, and then the corresponding one-dimensional MTF is [12]:

$$\begin{aligned} MTF(f) &= \mathscr{F}\left(LSF(x)\right) \\ &= \mathscr{F}\left(\sum_{y} PSF(x,y)\right) \\ &= \mathscr{F}\left(\sum_{z,y} DEP(x,y,z)\right) \end{aligned} \tag{1}$$

where f is the spatial frequency, and $\mathscr{F}$ denotes Fourier transform, and $DEP(x,y,z)$ here is obtained with a point

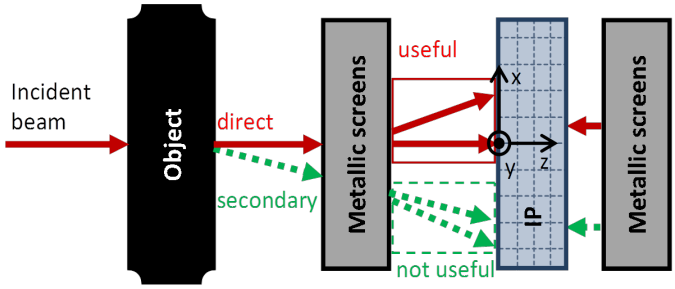

(a)

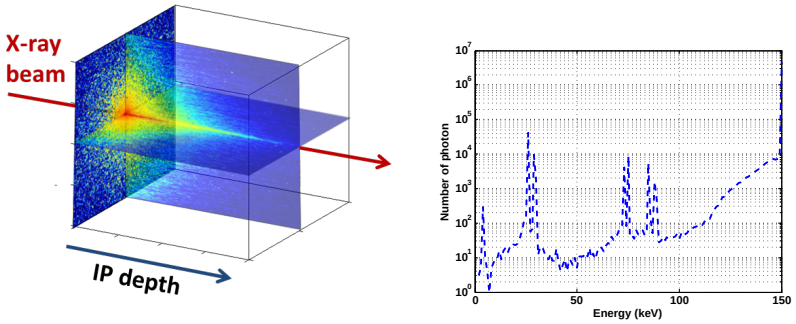

(b)

Figure 1: (a) The geometry adopted for our simulation is a classical radiography chain (not drawn to scale). A Cartesian coordinate system is used to track the particle transport. The y-axis points outward. A uniform three-dimensional orthogonal grid is applied to IP to record the deposited energy distribution. (b) Simulation outputs: 3D map of deposited energy in IP $DEP(x, y, z)$ and an example of spectrum after one of the elements between source and IP.

non-diverging source (pencil beam). The f_{MTF20} is the spatial frequency at which the MTF equals 20%. Depending on the investigation required, it is possible to consider the energy due to the different combinations of $useful/not\,useful$ and $photon/electron$.

- Energy absorption distribution along IP depth (EAD_z) and its centroid ($EADC$).
  An originality of our tool is to consider the distribution of deposited energy along the depth of IP (z direction). This is not common in other tools. Our idea is following: the latent image stored in IP (i.e. the deposited energy) is read by a laser light, and while the laser light enters IP, it diffuses along its traveling path due to the absorption, reflection and scattering effects, which contributes to image blurring. The laser power used during readout modifies the penetration of laser light, and thus, has an influence on final spatial resolution. Depending on the deposited energy profile along IP depth, an optimal laser power could be determined. For this reason, we would like to study the energy deposition distribution along the IP depth.
  The EAD_z is a function of z and is computed as the sum of $DEP(x, y, z)$ over x and y axes normalized by the incident beam energy.
  The centroid of EAD_z could be understood as the average position of the deposited energy, which is calculated using the following formula:

$$EADC = \frac{\sum_z z \cdot EAD_z(z)}{\sum_z EAD_z(z)} \qquad (2)$$

3. Context of our study: typical inspection case

Our typical industrial inspection case consists of irradiating a thick object (70 mm steel plate) with a high energy γ source (Cobalt). In order to explain the image quality issue, we show the result obtained when IP is used alone as a detector, without any metallic screen to intensify the signal. A pencil beam is used to irradiate the object, in order to show the spread out responsible for spatial resolution degradation. IP is placed directly behind the object, as in the industrial case.
Figure 2 illustrates the deposited energy images in XZ plane due to respectively the $useful$ photon signal (UPS), $useful$ electron signal (UES), $not\,useful$ photon signal (NUPS) and $not\,useful$ electron signal (NUES). Remember that z direction is the incident beam direction, and is limited to 150 μm, which is the thickness of the phosphor layer. As can be seen, the $useful$ signal images from photons and electrons are quite sharp and clear, while the $not\,useful$ signal images are blurry. In order to compare the amount of energy, in Figure 3, we plot the deposited energy along z direction for the respective signals. It is worth noting that the $not\,useful$ signals are dominant, as only about 15.7% of deposited energy is due to $useful$ signals. When looking at the depth penetration, we see that the electrons deposit their energy preferably towards the front side of IP ($z = 0$), while the photons near the rear side (z=150 μm).
In Figure 4, we investigate the contribution of the different signals to the overall MTF curve (dash-dotted line with point marker). Although the $useful$ signals UPS and UES have good MTFs (solid lines), the overall MTF is predominantly influ-

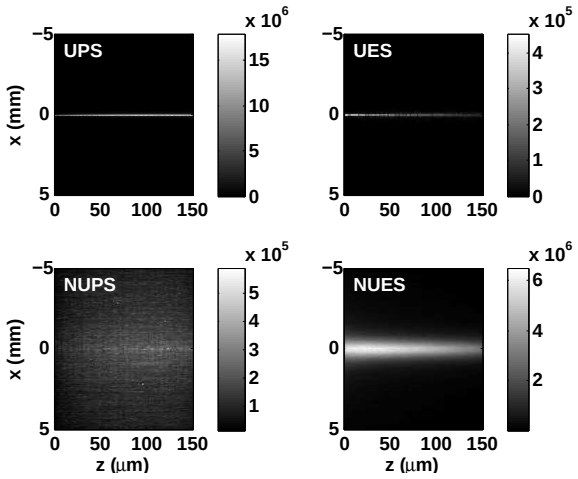

Figure 2: Deposited energy image in XZ plane, due to UPS, UES, NUPS and NUES.

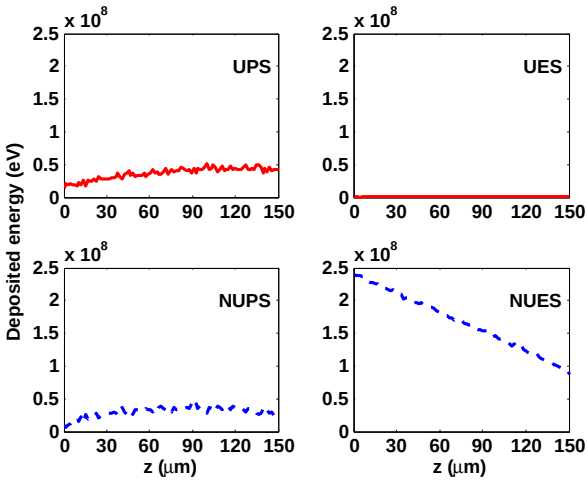

Figure 3: The deposited energy distributions along IP depth (z) respectively due to *useful* photon and electrons (UPS and UES), and *not useful* photons and electrons (NUPS and NUES).

enced by the *not useful* signals (NUPS, NUES). This is the quantitative aspect of the visual spread out already shown in Figure 2. It must be noted here that in real life, electrons might not have as much influence as what is shown here, because air was not considered in the simulation. However, this does not change the conclusion that *not useful* photons degrade a lot spatial resolution.

Thus, to conclude on our industrial context, we need a detector which should be efficient to the high energy *useful* signal, but insensitive to the lower energy *not useful* signal. The exact role of electrons must be very carefully tracked, as they might carry quite a lot of energy, but could be absorbed in the protective layer of IP itself. Thus, we see that a fine detector response characterization must be performed. A detailed analysis on the spectral and spatial response will be presented in the next section for physical phenomena comprehension and determination of optimal detector configuration.

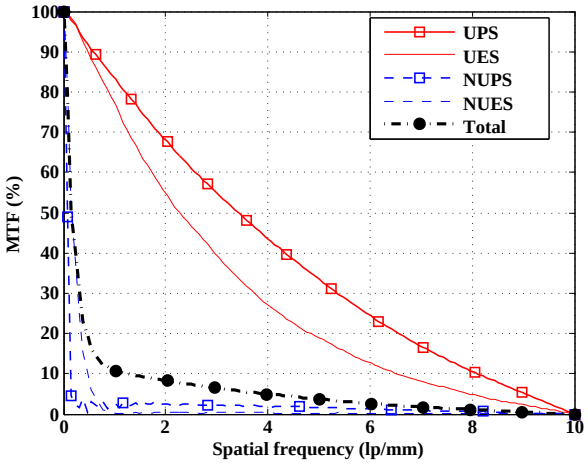

Figure 4: MTFs of the deposited energy image due to UPS, UES, NUPS and NUES, and the MTF of total deposited energy image.

4. Detector response characterization

We now investigate the impulse response of the system, which means the response to a pencil beam. All the elements (metallic screens and IP) were set cuboid, and no object is included in order to characterize only the detector system. The setting of all parameters is listed in Table 1. The incident number of photons is 10^7 for all the simulations considered in this section. Two combinations of screens were compared with *IP alone*. The first screen configuration (lead screen) is that requested by current standards. The second configuration (lead and tin) is chosen as an attempt to absorb K fluorescence of lead.

4.1. Spectral response analysis

4.1.1. Investigation of transmitted step-by-step spectra

In order to investigate the physical phenomena involved in each screen, we follow the photon spectrum after each step of the complete combination of screens (lead and tin). A monochromatic incident beam of 150 keV is chosen in such a way to be in the energy range where fluorescence occurs. Figure 5 illustrates the photon spectra:

- The first step in the detector system is the lead layer (asterisk) where it is visible that the initial monochromatic beam results in a continuous spectrum of secondary scattered radiation and fluorescence lines (K lines at 87, 84 and 74, 72 keV and L lines around 15 keV).
- The second step is the tin screen (dashed line): first of all it is observed that tin can effectively absorb the lead fluorescence (about 2 orders of magnitude) and also a big part of the scattered radiation between 30 and 80 keV. However, tin also yields its own fluorescence lines at around 30 keV.
- The last step corresponds to the protective layer of IP (plus sign): the overlapping of the dashed and cross marker curves indicates that no effect is introduced by the protective layer on the photon spectrum.

Table 1: Parameter setting. The IP was between the front and back screens, and the screens were placed in contact with IP

Elements			Configurations		
			IP alone	IP+0.2Pb	IP+0.2Pb0.8Sn
Source	Type:photon source		fixed energy	fixed energy	fixed energy
	Energy range in keV ($E_{min}, E_{max}, E_{incmt}$)		(2,1300,1)	(2,1300,1)	(2,1300,1)
Object	Object		none	none	none
Detector	Front screens		none	0.2mmPb	0.2mmPb +0.8mmSn
	IP	NbBX×NbBY×NbBZ	100×100×100	100×100×100	100×100×100
		Voxel dimension (μm^3)	10×10×1.5	10×10×1.5	10×10×1.5
	Back screens		none	0.2mmPb	0.8mmSn +0.2mmPb

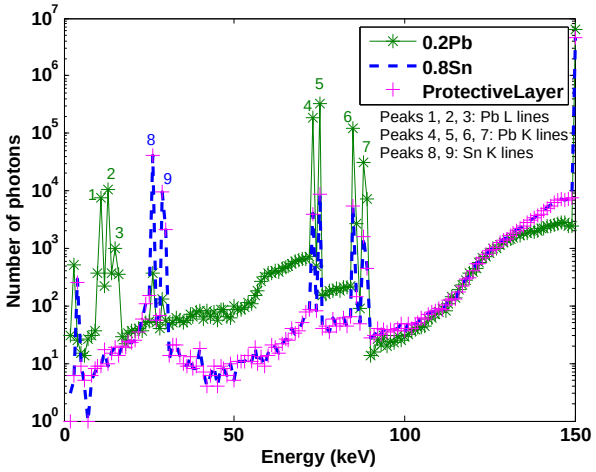

Figure 5: Step-by-step photon spectra obtained with Monte Carlo simulation.

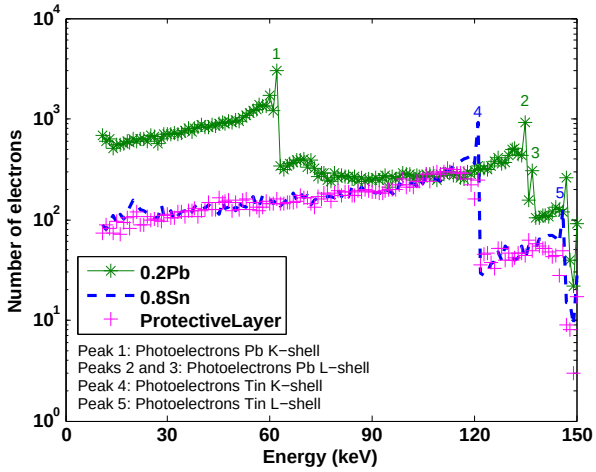

Figure 6: Step-by-step electron spectra obtained with Monte Carlo simulation.

Figure 6 shows the electron spectra after the different layers. In the photoelectric effect, an excitation photon of energy E is absorbed by the atom, which leads an excited atom and a photoelectron leaving the atom with a kinetic energy $E_k = E - U_i$, where U_i is the ionization energy of the electron [22].

- The first step (asterisk) represents the electron spectrum after the lead screen, where two peaks are visible, respectively at 62 keV and 135 keV, corresponding to the photoelectrons coming from the lead K-shell (whose ionization energy is about 88 keV) and L-shell (whose ionization energy is about 15 keV).

- After the tin layer (whose K- and L-shell ionization energies are about 29 keV and 4 keV respectively), the photoelectron peaks are observed at 121 keV and 146 keV (dashed line).

- When comparing the spectra after tin (dashed line) and after the protective layer (plus sign), we can observe that the photoelectron peaks are much reduced, but overall, the energy stopped by the protective layer is negligible with respect to the total incident energy into this layer. Thus, in this energy range, the protective layer do not prevent electrons from entering the phosphor layer.

The study of the spectra is illustrative and helps to understand phenomena, but for high energies, a more global study of absorption efficiency is needed.

4.1.2. Energy absorption efficiency

Figure 7(a) shows the energy absorption efficiency plots of the 3 different detector configurations.

- The response of *IP alone* (solid line) is quite efficient, nearly 1, at low energies, but with the increase of excitation energy, the curve drops quickly towards zero. The small rise occurring between 20 and 30 keV corresponds to the barium absorption edge.

- The lead screen (dashed line) filters the low energy radiation but intensifies the high energies: the dashed curve is above the curve of *IP alone* for energies greater than 131 keV. The barium absorption edge has disappeared due to the filtering of low energies. At around 89 keV a quick drop arises which is due to the strong K-absorption of lead.

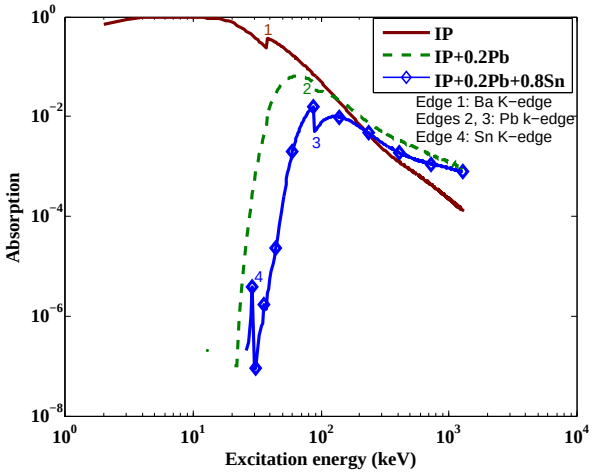

(a)

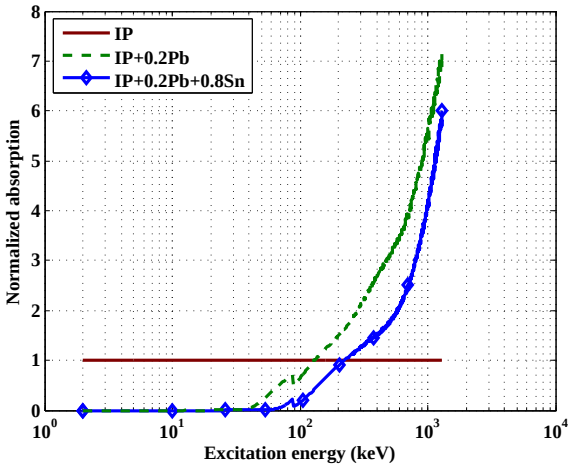

(b)

Figure 7: (a) The photon absorption efficiency as a function of energy for different detector configurations and (b) the absorption efficiency curves of different detector configurations normalized by that of *IP alone*.

- With the combination of lead and tin screens (solid line with diamond markers), similar effects are observed, except that the signal intensification starts from 226 keV, and an additional drop appears at 30 keV which corresponds to the K-absorption of tin.

In order to compare the intensification effect of the different combinations of metallic screens, the absorption curves of the two configurations were normalized by that of *IP alone* (Figure 7(b)). Starting from 131 and 226 keV respectively, the two kinds of screen combinations intensify the absorbed signal in IP (normalized absorption to 1), and the intensification increases continuously. Regarding only the absorption intensification in the high energy range, the detector configuration with only lead is preferred, as it has the highest absorption level among the three. However, the tin plus lead combination has a better filtering of low energies. Thus, when considering the compromise introduced in section 3, namely the need to increase high energy weight (in order to absorb the *useful* signal) and avoiding the low energy *not useful* signal, the two screen combinations can be discussed (see section 5). On the other hand, the spatial resolution must also be compared, which is the aim of the next section.

4.2. Spatial response analysis

4.2.1. MTF curve and the limit of resolution at 20% MTF (f_{MTF20})

Figure 8(a) shows the MTF curves of the *IP alone* for different excitation energies. In the low to medium energy range (see dark blue curves, up to about 400 keV), the MTF curve drops quickly with the increase of excitation energy, whereas, in the high energy range (see light blue to dark red curves, 400 keV to 1300 keV), the MTF curves overlap each other, meaning that the spatial resolution could be considered energy independent in this high energy range. Two gaps appear at 14 keV and 38 keV resulting from the K fluorescence reabsorption of brome and barium, as the fluorescence emission is isotropic, and thus, the PSF spreads out.

Figure 8(b) is the plot of f_{MTF20} versus excitation energy for *IP alone*. The two slumps correspond again to the K fluorescence reabsorption of brome and barium (like the two gaps just described above). As the excitation energy continues to increase, exceeding the K-edge energy, less fluorescence is produced, so less K fluorescence reabsorption, and hence the limit of resolution improves right after the K-edges, which was difficult to see in Figure 8(a) due to the color scale.

Figure 9 compares the resolution of the three detector configurations. With the lead screens on both sides of IP, a degradation of spatial resolution is introduced, especially at 89 keV, at which the fluorescence of the lead starts to yield. As a photon with a higher energy has a larger free traveling path, the lead fluorescence could spread further than that of barium and brome, and hence the resolution drop is much greater at 89 keV than it is at 14 and 38 keV. At energies lower than 89 keV, the addition of a tin screen between lead and IP further degrades the resolution since it is another layer spreading the incident beam. However, when the excitation energy exceeds 89 keV, as

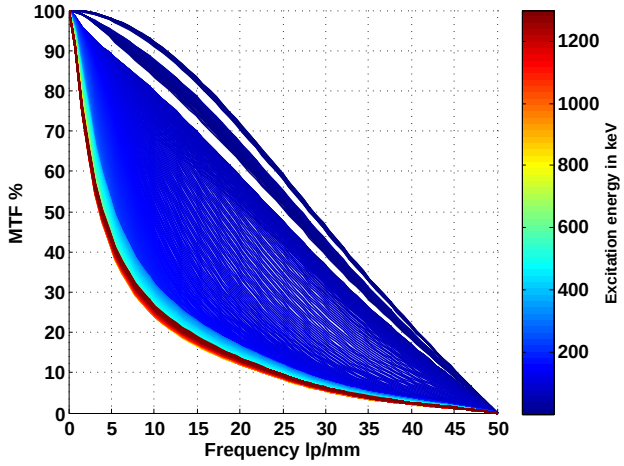

(a)

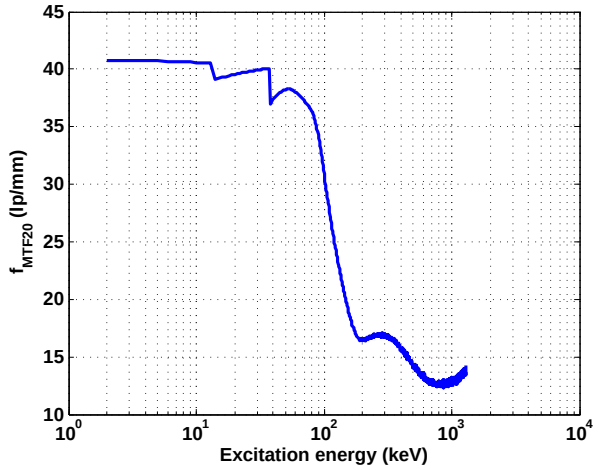

(b)

Figure 8: (a) MTF curves at different excitation energies for IP alone and (b) the f_{MTF20} versus excitation energy. (For interpretation of the references to color in this figure legend, the reader is referred to the web version of this article.)

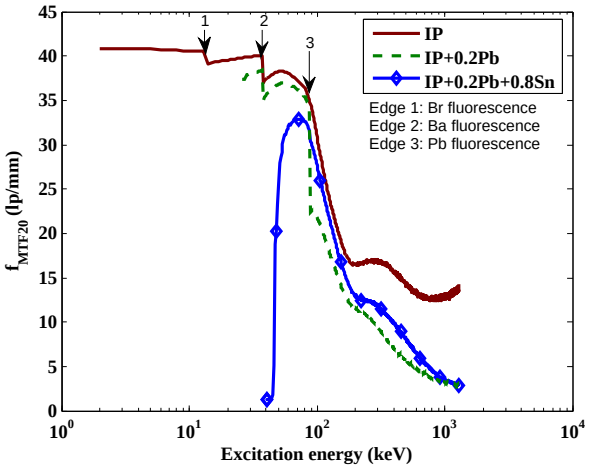

Figure 9: The f_{MTF20} versus excitation energy for different detector configurations.

the lead fluorescence could be effectively attenuated by the tin screen (Figure 5), the resolution improves. This improvement, however, decreases as the excitation energy continues increasing, and becomes negligible at 1300 keV.

As a conclusion of this part, even considering only spatial resolution, it is difficult also to choose the best screen configuration because the behavior respectively at low to medium and high energies is not the same, and both should be considered for our typical industrial case.

4.2.2. The energy absorption distribution along z (EAD_z) and its centroid (EADC)

Now we would like to investigate the energy deposition with respect to the IP depth (z direction).

Figure 10(a) is a 2D visual image of energy absorption (in a color scale) as a function of excitation energy in abscissa, while the IP depth is represented in the vertical direction, with the front side at $z = 0$ and the rear side at $z = 150\,\mu$m. First of all, it is very clear that absorption is better in the low energy range (red color is only near 0 keV), and most of the energy is deposited towards the front side of IP.

In order to have a better visualization of the influence of z direction, Figure 10(b) shows the profile of energy deposition along z, EAD_z, at 20, 40, 100 and 1000 keV. We see that when excitation energy is small, the deposited energy is mostly near the front surface of IP, while with the increase of the excitation energy, the distribution is more and more towards the rear surface. The dropping at the boundaries is probably due to particle escaping.

In order to facilitate the comparison, we plot the centroid $EADC$ versus excitation energy in Figure 11. In our case, the centroid value is between 0 and 150 μm, where 0 μm means that all energy is deposited at the front surface of IP, and 150 μm the rear surface. When viewing the response of *IP alone*, at low energies, the energy is preferentially deposited on the front side, and with the increase of excitation energy, the energy tends to be deposited towards the rear side so that the centroid value in-

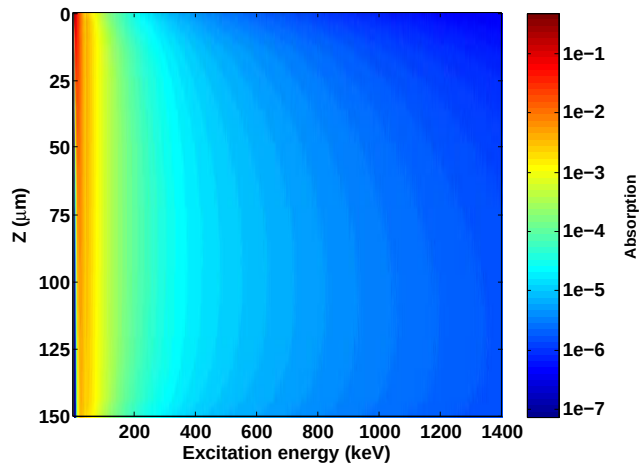

(a)

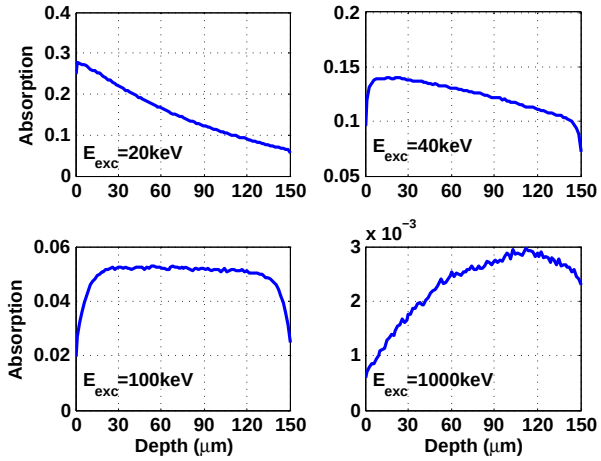

(b)

Figure 10: (a) 2D visual of absorption versus IP depth and excitation energy and (b) the EAD_z at 20, 40, 100 and 1000 keV. 0 μm is the front side of IP and 150 μm the rear side. (For interpretation of the references to color in this figure legend, the reader is referred to the web version of this article.)

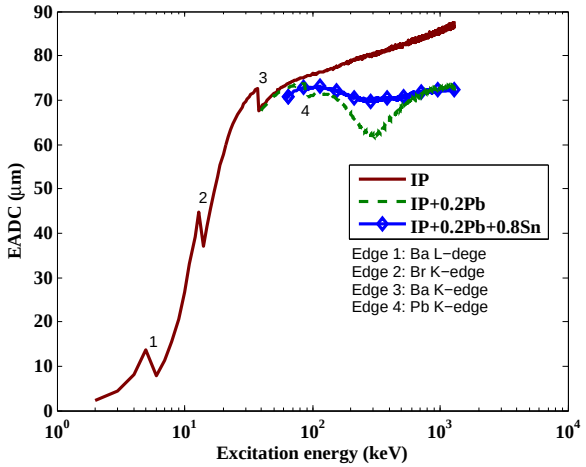

Figure 11: The *EADC* versus excitation energy for different detector configurations.

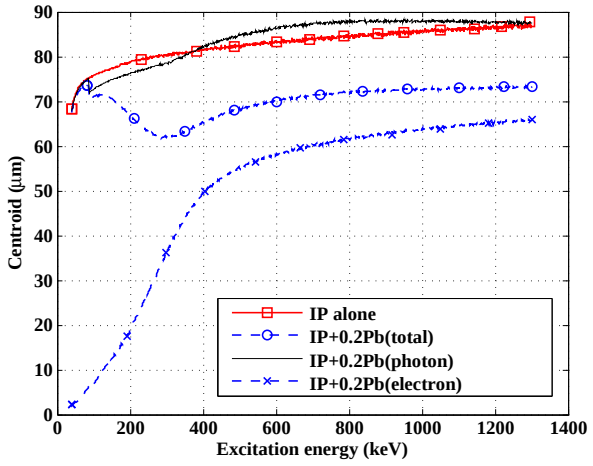

(a)

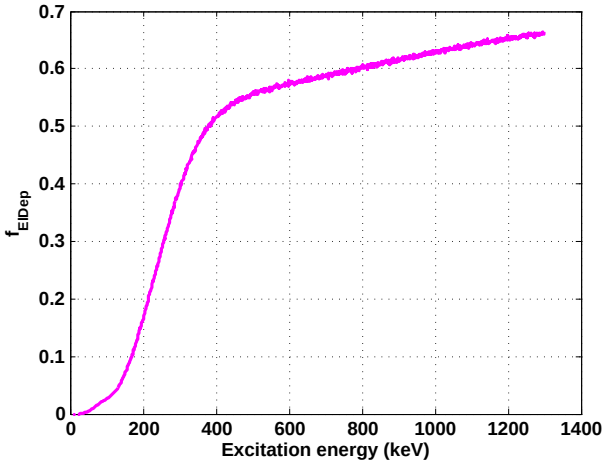

(b)

Figure 12: (a) The photon and electron beam EADCs for $IP + 0.2Pb$, as well as the total EADC for $IP + 0.2Pb$ and $IPalone$, and (b) the f_{ElDep} varying as a function of excitation energy for $IP + 0.2Pb$.

creases.

When comparing screens with *IP alone*, we see that the centroid is shifted towards the front side to a different extent. Similarly to the absorption efficiency and sharpness measurements, it is also observed a sudden change due to the K-absorptions of fluorine, brome and barium in the solid line, and lead in the dashed line. When comparing both screens, a small decrease of the centroid is observed with only the lead screen, which must be elucidated. It must be noted that the centroid investigation is important because the laser readout process is usually done from the front side of the IP and limited to a small depth. Thus, if we show that the centroid is lower, there is an interest for a best readout process.

As an attempt to elucidate the decrease in the centroid distribution with lead, in Figure 12(a), we study separately the centroid obtained for the photon and electron beams: the photon beam *EADC* curve overlaps the *EADC* curve of *IP alone*, whereas the electron beam *EADC* is closer to the front surface, and it increases with excitation energy. Here we see that the electron

beam is mostly responsible for shifting the deposited energy towards the front side, but the degree of the shift depends on the fraction of the deposited energy which is due to electron beam. Thus, in Figure 12(b) we plot the fraction of the deposited energy due to the electron beam (f_{ElDep}): the f_{ElDep} also increases with excitation energy and at energies over 400 keV, more than half of the deposited energy comes from the electrons emerging from the lead screen. Thus, when comparing lead screen with *IP alone*, at low energies, even though the electron beam centroid is very close to zero, as the fraction of deposited energy is small, no obvious shift is observed; with the increase of excitation energy, the centroid shift could be observed, and the optimal centroid is at around 300 keV, an energy for which the electron beam centroid is still small and the fraction of deposited energy is important.

5. Results: industrial case optimization

According to the detailed analysis in the previous part, we find that both the two detector configurations with metallic screens could increase the $useful$ signal weight in the final image since they could effectively increase the absorption efficiency at high energies and eliminate the influence of low energy signal, especially $IP + 0.2Pb0.8Sn$ which has better filtering effect at low energies. While limiting the blurring introduced by $not\,useful$ signal, the screens also degrade the spatial resolution, therefore, a suitable detector should provide good $useful$ to $not\,useful$ signal ratio without losing much spatial resolution.

As experiments, the outcome of a Monte Carlo code is affected by statistical uncertainty, which is directly related to the number of photons involved in the process. The greater the number of incident photons, the less the relative uncertainty. The error is usually estimated as three times the standard deviation of the deposited energy. In our case, the number of initial photons has been chosen in order that this error is relatively small. In Figure 13 we show the $useful$ over $not\,useful$ signal ratio: the ratio is greatly improved with $IP + 0.2Pb0.8Sn$. The incident photon numbers of the three configurations are respectively 6×10^8, 3×10^8 and 3×10^8. In Figure 14 we see that the MTF with $IP+0.2Pb$ (Figure 14(a)) and with $IP+0.2Pb0.8Sn$ (Figure 14(b)) are nearly the same. Comparing the spatial frequency at 20% MTF, $IP + 0.2Pb0.8Sn$ ($1.62\,lp/mm$) is a little better than $IP + 0.2Pb$ ($1.45\,lp/mm$). Hence $IP + 0.2Pb0.8Sn$ is overall better for our industrial case.

6. Discussion

Through the IP response characterization and a detailed analysis on the spectral and spatial responses, we optimized an inspection case. IP+$0.2Pb0.8Sn$ is the overall preferable detector configuration since it increases the most the high energy $useful$ signal weight without losing too much the energy absorption efficiency and spatial resolution.

From the performed study, we find that the metallic screens could: enhance the high energy signal and filter the low energy signal, degrade spatial resolution (the fluorescence of the

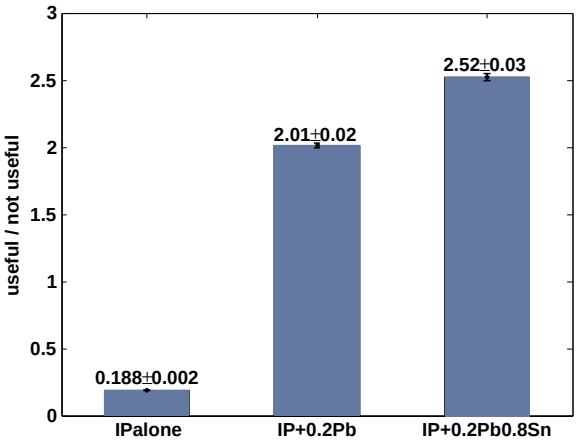

Figure 13: The ratio of $useful$ over $not\,useful$ signal.

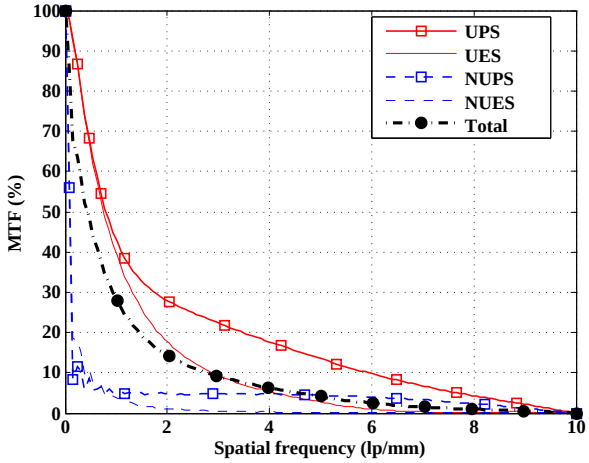

(a)

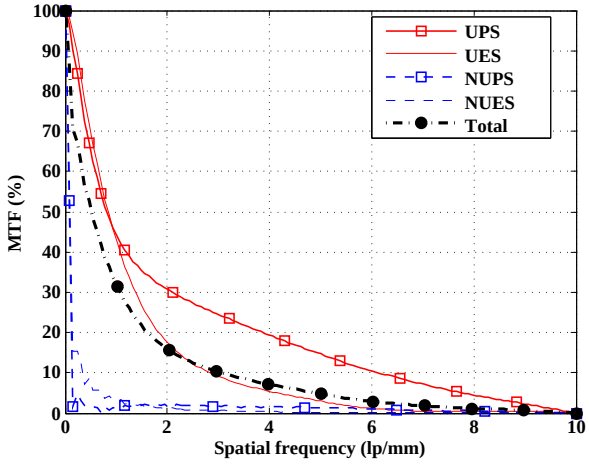

(b)

Figure 14: MTFs of the deposited energy image due to different signals for: (a) $IP + 0.2Pb$ and (b) $IP + 0.2Pb0.8Sn$.

screens is crucial), and shift the deposited energy toward the front surface of IP. The electron beam is mostly responsible for shifting the energy deposition distribution, and the degree of the shift depends on both the fraction and the centroid of the deposited energy due to electron produced by the metallic screens.

7. Conclusion

In this paper, we presented a Monte Carlo simulation tool for investigating the physical phenomena involved in the energy deposition process in IP. This tool allows different case studies on understanding the experimental observations and optimizing the image quality and choose the best IP/screen combination. This tool also provides the evaluation of the spectra transmitted along the different elements so that the fluorescence and scattered radiation production could be monitored as well as the influence of the protective layer of the IP.
As a future work, a comparison between experimental and simulation results of the detector performance (i.e. spectral and spatial response) will be of great interest.
The IP response characterization results obtained by this simulation tool will be applied to our future work on CR imaging chain modeling and optimization.

References

[1] M. Sonoda, M. Takano, J. Miyahara, H. Kato, Computed radiography utilizing scanning laser stimulated luminescence, Radiology 148 (3) (1983) 833–838.

[2] J. A. Rowlands, The physics of computed radiography, Physics in medicine and biology 47 (23) (2002) R123–166.

[3] H. v. Seggern, Photostimulable X-ray storage phosphors: a review of present understanding, Brazilian journal of physics 29 (2) (1999) 254–268.

[4] J. Miyahara, K. Takahashi, Y. Amemiya, N. Kamiya, Y. Satow, A new type of X-ray area detector utilizing laser stimulated luminescence, Nuclear Instruments and Methods in Physics Research Section A: Accelerators, Spectrometers, Detectors and Associated Equipment 246 (1–3) (1986) 572–578.

[5] M. Thoms, The quantum efficiency of radiographic imaging with image plates, Nuclear Instruments and Methods in Physics Research Section A: Accelerators, Spectrometers, Detectors and Associated Equipment 378 (3) (1996) 598–611.

[6] M. Thoms, The dynamic range of X-ray imaging with image plates, Nuclear Instruments and Methods in Physics Research Section A: Accelerators, Spectrometers, Detectors and Associated Equipment 389 (3) (1997) 437–440.

[7] EN14784-2, Non-destructive testing - Industrial computed radiography with storage phosphor imaging plates - Part 2: General principles for testing of metallic materials using X-rays and gamma rays, 2005.

[8] ISO17636-2, Non-destructive testing of welds – Radiographic testing – Part 2: X- and gamma-ray techniques with digital detectors, 2009.

[9] D. W. O. Rogers, Fifty years of Monte Carlo simulations for medical physics, Physics in medicine and biology 51 (13) (2006) R287–301.

[10] J. M. Boone, J. A. Seibert, J. M. Sabol, M. Tecotzky, A Monte Carlo study of X-ray fluorescence in X-ray detectors, Medical physics 26 (6) (1999) 905–916.

[11] S. Correa, E. Souza, A. Silva, D. Cassiano, R. Lopes, Computed radiography simulation using the Monte Carlo code MCNPX, Applied Radiation and Isotopes 68 (9) (2010) 1662–1670.

[12] P. F. Liaparinos, I. S. Kandarakis, D. A. Cavouras, H. B. Delis, G. S. Panayiotakis, Monte Carlo study on the imaging performance of powder $Lu_2SiO_5 : Ce$ phosphor screens under X-ray excitation: Comparison with $Gd_2O_2S : Tb$ screens, Medical Physics 34 (5) (2007) 1724.

[13] C. Kausch, B. Schreiber, F. Kreuder, R. Schmidt, O. Dossel, Monte Carlo simulations of the imaging performance of metal plate/phosphor screens used in radiotherapy, Medical Physics 26 (10) (1999) 2113–2124.

[14] D. A. Jaffray, J. J. Battista, A. Fenster, P. Munro, Monte Carlo studies of X-ray energy absorption and quantum noise in megavoltage transmission radiography, Medical Physics 22 (7) (1995) 1077–1088.

[15] P. F. Liaparinos, I. S. Kandarakis, D. A. Cavouras, H. B. Delis, G. S. Panayiotakis, Modeling granular phosphor screens by Monte Carlo methods, Medical Physics 33 (12) (2006) 4502–4514.

[16] P. F. Liaparinos, I. S. Kandarakis, The Monte Carlo evaluation of noise and resolution properties of granular phosphor screens, Physics in Medicine and Biology 54 (4) (2009) 859–874.

[17] E. M. Souza, S. C. A. Correa, A. X. Silva, R. T. Lopes, D. F. Oliveira, Methodology for digital radiography simulation using the Monte Carlo code MCNPX for industrial applications, Applied radiation and isotopes: including data, instrumentation and methods for use in agriculture, industry and medicine 66 (5) (2008) 587–592.

[18] H. H. Li, A. L. Gonzalez, H. Ji, D. M. Duggan, Dose response of $BaFBrI : Eu^{2+}$ storage phosphor plates exposed to megavoltage photon beams, Medical physics 34 (1) (2007) 103–111.

[19] G. Cho, H. Kim, Y. Chung, D. K. Kim, H. Lee, T. Suh, K. Joo, Monte Carlo analyses of X-ray absorption, noise and detective quantum efficiency considering therapeutic x-ray spectrum in portal imaging detector, in: 2000 IEEE Nuclear Science Symposium Conference Record, Vol. 3, 2000, pp. 19/64–19/68 vol.3.

[20] S. Wu, X. Jin, C. Xie, G. Cao, Optimal steel thickness combined with computed radiography for portal imaging of nasopharyngeal cancer patients, Medical Physics 32 (10) (2005) 3112–3116.

[21] S. G. PENELOPE 2008, J. M. Fernández Varea, J. Sempau Roma, Organització de Cooperació i Desenvolupament Econòmic, PENELOPE 2008: A code system for Monte Carlo simulation of electron and photon transport : workshop proceedings, barcelona, spain 30 june-3 july 2008, OECD, 2009.

[22] J. Beutel, H. L. Kundel, R. L. Van Metter (Eds.), Hand book of medical imaging: Volume 1. Physics and Psychophysics, SPIE Press, 2000, Ch. 1. X-ray Production, Interaction, and Detection in Diagnostic Imaging.